

A MULTI-FREQUENCY RADIO STUDY OF SUPERNOVA REMNANT G292.0+1.8 AND ITS PULSAR WIND NEBULA

B. M. GAENSLER¹ AND B. J. WALLACE²

Accepted to The Astrophysical Journal on 09-May-2003

ABSTRACT

We present a detailed radio study of the young supernova remnant (SNR) G292.0+1.8 and its associated pulsar PSR J1124–5916, using the Australia Telescope Compact Array at observing wavelengths of 20, 13 and 6 cm. We find that the radio morphology of the source consists of three main components: a polarized flat-spectrum central core coincident with the pulsar J1124–5916, a surrounding circular steep-spectrum plateau with sharp outer edges and, superimposed on the plateau, a series of radial filaments with spectra significantly flatter than their surroundings. H I absorption argues for a lower limit on the distance to the system of 6 kpc.

The core clearly corresponds to radio emission from a pulsar wind nebula powered by PSR J1124–5916, while we conclude that the plateau represents the surrounding SNR shell. The plateau’s sharp outer rim delineates the SNR’s forward shock, while the thickness of the plateau region demonstrates that the forward and reverse shocks are well-separated. Assuming a distance of 6 kpc and an age for the source of 2500 yr, we infer an expansion velocity for the SNR of $\sim 1200 \text{ km s}^{-1}$, an ambient density $\sim 0.9 \text{ cm}^{-3}$, an ejected mass $\sim 5.9 M_{\odot}$ and a supernova explosion energy $\sim 1.1 \times 10^{51} \text{ erg}$. We interpret the flat-spectrum radial filaments superimposed on the steeper-spectrum plateau as Rayleigh-Taylor unstable regions between the forward and reverse shocks of the SNR. The flat radio spectrum seen for these features results from efficient second-order Fermi acceleration in strongly amplified magnetic fields. Overall, SNR G292.0+1.8 shows an unusual set of properties not seen in any other SNR. This source may reflect a unique stage in evolution, only seen for systems at an age of $\sim 2500 \text{ yr}$, and only for which there is both a bright SNR shell and an energetic associated pulsar.

Subject headings: ISM: individual: (G292.0+1.8) — pulsars: individual (J1124–5916) — stars: neutron — ISM: supernova remnants — radio continuum: ISM

1. INTRODUCTION

When a massive star ends its life in a supernova explosion, the expectation has been that this should leave behind an expanding supernova remnant (SNR) with oxygen-rich ejecta, a central neutron star observable as a radio pulsar, and a synchrotron-emitting pulsar wind nebula (PWN) powered by the rotating neutron star. However, as yet only one system in the Galaxy has been identified which has all these properties: the SNR G292.0+1.8 (also known as MSH 11–54) and its associated pulsar, PSR J1124–5916. These sources thus present an ideal opportunity to study the aftermath of a core-collapse supernova, and the resulting interaction of its products with the interstellar medium (ISM) and with each other.

G292.0+1.8 was first detected through its radio emission (Mills, Slee, & Hill 1961). On the basis of its non-thermal radio spectrum and lack of recombination lines (Milne 1969; Wilson et al. 1970), G292.0+1.8 was subsequently classified as a SNR, while H I absorption showed it to be at a distance of at least 3.7 kpc (Caswell et al. 1975). The first sub-arcminute resolution image of the SNR revealed a filled-center radio morphology (Lockhart et al. 1977), which led to its classification as a “Crab-like” SNR, i.e. its emission was interpreted as being dominated by that from a PWN, rather than from the surrounding SNR ejecta and their interaction with the ISM. However, more sensitive radio observations demonstrated the SNR to be composed of both a bright central ridge and a surrounding plateau (Braun et al. 1986). This led Braun et al. (1986) to reinterpret the SNR as a thick shell interacting with dense material,

with no pulsar-powered component.

The classification of G292.0+1.8 as a “shell-type” SNR was supported by observations in other wavebands. In the optical, high-velocity oxygen rich filaments were identified, characteristic of emission from a young SNR with a massive progenitor (Goss et al. 1979; Murdin & Clark 1979; van den Bergh 1979; Braun et al. 1983), and arguing for an age $\sim 1700 \text{ yr}$. In X-rays, the SNR showed an ellipsoidal disk of emission (Tuohy, Clark, & Burton 1982), with an emission-line spectrum resulting from the shock-heated ejecta of a massive progenitor (Clark, Tuohy, & Becker 1980; Hughes & Singh 1994). The SNR also showed extensive infra-red emission resulting from shock-heated dust (Braun et al. 1986). Until a few years ago, it thus seemed clear that SNR G292.0+1.8 was a shell SNR, with no known central pulsar or PWN.

New telescopes with imaging capabilities in hard X-rays have revised this classification. *ASCA* observations of this source lacked high spatial resolution, but clearly showed there to be a hard, compact X-ray source embedded in extended softer emission from the rest of the SNR (Torii, Tsunemi, & Slane 1998) — this region of harder emission was interpreted as X-ray synchrotron emission from a central PWN. High-resolution observations of SNR G292.0+1.8 with the *Chandra X-ray Observatory* dramatically confirmed this claim, demonstrating the presence of a filled-center X-ray PWN, $1' - 2'$ across, slightly offset from the center of the surrounding SNR (Hughes et al. 2001). These observations also revealed a point-like source within the PWN, which Hughes et al. (2001) argued

¹Harvard-Smithsonian Center for Astrophysics, 60 Garden Street MS-6, Cambridge, MA 02138; bgaensler@cfa.harvard.edu

²Defence R&D Canada — Ottawa, 3701 Carling Avenue, Ottawa, ON, K1A 0Z4, Canada; Brad.Wallace@drdc-rddc.gc.ca

was the central powering pulsar. A deep search for pulsations at this position, using the Parkes radio telescope, has indeed resulted in the detection of a radio pulsar, PSR J1124–5916, at this position (Camilo et al. 2002); the pulsar has a spin-period of 135 ms, a spin-down luminosity of 1.2×10^{37} erg s⁻¹ and a characteristic age of 2900 yr, properties all consistent with it being the young neutron star associated with the coincident SNR. Pulsations have since been detected from this source in X-rays also (Hughes & Slane 2003).

It is thus now clear that SNR G292.0+1.8 is a “composite” SNR, clearly showing a SNR blast-wave, a central pulsar and a PWN. We here present an extensive multi-frequency study of the radio emission from G292.0+1.8 using the Australia Telescope Compact Array (ATCA), the observations for which are of far higher angular resolution and sensitivity, and the spectral coverage much broader, than any existing radio studies of this source. The aims of this experiment are to properly characterize the morphological and spectral properties of the radio emission from the SNR and its PWN, to constrain the distance to the source, and to compare the radio and X-ray properties of the SNR. In §2 we summarize our observations and analysis of the radio data, in §3 we describe the resulting images, HI absorption and spectral index distribution for this source, and in §4 we interpret these data in the context of the distance to the source, and the properties of the SNR and PWN.

2. OBSERVATIONS AND ANALYSIS

Observations of SNR G292.0+1.8 were carried out with the ATCA (Frater, Brooks, & Whiteoak 1992), a six-element synthesis telescope located near Narrabri, NSW, Australia. These observing runs utilized a variety of array configurations and observing frequencies, summarized in Table 1. Each observation consisted of a dual-frequency 12-hour synthesis. Continuum observations were carried out at wavelengths of 20 cm (center frequencies of 1375, 1344 and 1472 MHz), 13 cm (2240 and 2496 MHz) and 6 cm (4800, 5056, 5312 and 5440 MHz), as listed in Table 1; multiple center frequencies were used within each waveband to improve the $u-v$ coverage of the observations. All continuum observations used 32 channels recorded across a 128-MHz continuum band, and included data in all four Stokes parameters. Spectral line observations were carried out centered on the 1420-MHz HI line, and consisted of 1024 channels across a 4-MHz band; only total intensity was recorded in these data. Observations of G292.0+1.8 at 20 and 13 cm, and in the HI line, were carried out in a single pointing offset from the SNR by a few arcmin, so as to prevent artifacts at the phase center from corrupting the image. Observations at 6 cm consisted of a 3-point mosaic centered on the SNR. The shortest array spacing in each waveband was 31 meters, corresponding to a maximum angular scale to which the array was sensitive of $\sim 24'$ and $\sim 14'$ at 20 and 13 cm respectively. At 6 cm, the mosaicing process allowed us to recover somewhat shorter spacings (Ekers & Rots 1979), so that we can image scales as large as $\sim 10'$. In all cases, the array was sensitive to all scales on which emission is expected to be produced by the SNR, down to the resolution limit.

Flux calibration for all observations was carried out using data taken on PKS B1934–638.³ Antenna gains and polarization calibration were measured using regular observations of either PKS B1105–680 or PKS B1148–671, as indicated in Table 1. Data were edited and calibrated using the MIRIAD pack-

age (Sault & Killeen 1999). During this reduction, it became apparent that the 20-cm observations of PKS B1105–680 contained significant extended structure. To determine the time-variation in the complex antenna gains we used self-calibration to produce a high-fidelity image of this calibration field, and then applied the resulting gain solutions to G292.0+1.8.

Total intensity images at 20, 13 and 6 cm were formed using multi-frequency synthesis to maximize $u-v$ coverage, and with uniform visibility weighting so as to minimize sidelobes. The 20-cm image was formed from all available data, while the images at 13 and 6 cm excluded all baselines longer than 3 km so as to boost signal-to-noise and to match the resolution of the 20-cm data. Each image was deconvolved using a maximum entropy algorithm; the 6-cm mosaic fields were all deconvolved simultaneously using the MOSMEM algorithm (Sault, Staveley-Smith, & Brouw 1996). Each image was then smoothed with a gaussian restoring beam (the dimensions of which are listed in Table 2), and then corrected for the mean primary beam response of the antennas.

A compact source embedded in G292.0+1.8, at position (J2000) RA 11^h24^m25^s.19, Dec $-59^\circ 13'46''.4$, appears to have varied in its flux density between epochs and consequently produces sidelobes which corrupt the images. At each epoch, we have consequently subtracted the Fourier transform of this source out of the $u-v$ data before making the image from the combined data-sets. Once these data had been successfully deconvolved and restored, we added back to the image an unresolved source at this position with the appropriate mean flux density.

Images in Stokes Q , U and V were similarly formed in each waveband. At 20 and 13 cm these images were deconvolved using the CLEAN algorithm, while at 6 cm we used the PMOSMEM algorithm (Sault, Bock, & Duncan 1999). Q and U images in each waveband were then combined to form images of polarized intensity and polarized position angle; a correction for the Ricean bias was applied to these data. Examination of the polarized position angles on a channel-by-channel basis within the 13 cm band (see Gaensler, Manchester, & Green 1998) demonstrated that the rotation measure (RM) towards the SNR is low, typically $|RM| \lesssim 30$ rad m⁻². There is thus only $\sim 20^\circ$ of Faraday rotation between the 13 and 6 cm data. We thus directly compared these two data-sets to correct for Faraday rotation and derive the intrinsic polarized position angles, without concern as to possible ambiguities between wavebands.

To properly compare interferometric data-sets at different wavelengths and thus determine spectral indices, one must first ensure that the corresponding images are matched in $u-v$ coverage. We thus re-sampled the 20 cm observations so that they matched the 13 cm and 6 cm data in their $u-v$ sampling, primary beam shape and mosaicing pattern, and similarly re-sampled the 13 cm data to match the 6 cm data (see Gaensler et al. 1999). The re-processed data-sets were then imaged and deconvolved in identical fashion as to the data to which they had been matched. This produced three pairs of images (20/13, 20/6 and 13/6) which were identical in their spatial sampling and fidelity, and differed only in their brightness distributions. These images could then be directly compared.

For the HI data, we subtracted the continuum contribution to the visibilities in the $u-v$ plane using the UVLIN algorithm (Sault 1994). Cubes of emission were then formed for each

³see http://www.narrabri.atnf.csiro.au/observing/users_guide/html/node215.html

spectral line, in which the 1024 visibility channels were rebinned to form 207 channels each of velocity width 1.7 km s^{-1} , ranging between -100 and $+250 \text{ km s}^{-1}$. In the HI line, we enhanced our surface-brightness sensitivity by only using baselines shorter than 1200 m to make our images. The resulting cubes were deconvolved using 1000 iterations of the CLEAN algorithm, and then restored with a gaussian beam. In the HI line, we extracted absorption spectra by weighting the cube by the 20-cm continuum emission from the same region, averaging the spectrum over a particular region of interest, and then normalizing appropriately to give units of fractional absorption. We determined the absorption threshold above which a feature is regarded as significant by measuring the rms fluctuations in line-free channels, and adopting a value six times higher than this as our sensitivity limit. We adopt a factor of six to reflect the increased system temperature in the HI line (e.g. Dickey 1997).

3. RESULTS

3.1. Imaging and Radio/X-ray Comparison

Radio images of G292.0+1.8 at 20, 13 and 6 cm (without any filtering applied to match the range of spatial scales measured in each case) are shown in Figure 1, while a slice through the SNR is shown in Figure 2. These data clearly demonstrate that the morphology of G292.0+1.8 is comprised of at least two components, confirming similar claims made from lower resolution data (Lockhart et al. 1977; Braun et al. 1986). Concentric with the SNR center, approximately circular, and with an angular diameter of $4'$, is a bright centrally-filled region, which we follow previous authors in referring to as the “core”. PSR J1124–5916 is within this region, offset by $\sim 30''$ to the south-east of the core’s center. The brightest part of the core has a ridge-like morphology, primarily elongated east-west. As shown in the lower-right panel of Figure 1, this ridge runs just to the north of the pulsar.

Surrounding the core is a fainter region of diameter $8'$. This region, which Lockhart et al. (1977) designated the “plateau”, is somewhat brighter on its western half compared to the eastern side of the source. Figure 2 demonstrates that the plateau has sharp outer edges, over which the surface brightness drops to that of the background in less than a single beamwidth. The circumference of the plateau in some places shows several straight-edged segments, rather than a single curved perimeter. This is most striking along the eastern and north-eastern edges of the source.

To determine the flux density for the entire SNR, we measured the flux within a circle centered on RA (J2000) $11^{\text{h}}24^{\text{m}}34.^{\text{s}}2$, Dec. (J2000) $-59^{\circ}15'54''$ with radius $288''$. We determined the background for this region by measuring the flux in an annulus of the same center, and with inner/outer radii $288''/370''$. We similarly measured the flux density of the core region, using a circle and annulus centered on RA (J2000) $11^{\text{h}}24^{\text{m}}37.^{\text{s}}6$, Dec. (J2000) $-59^{\circ}15'55''$, with circle radius $126''$, and annular inner/outer radii $126''/164''$. The flux for the plateau is then that of the whole source less that of the core. The resulting measurements at each wavelength are given in Table 2.

A number of smaller-scale radio features can be seen superimposed on the plateau region. Most prominent are two spurs of emission south-west of the center; fainter radial filaments can be seen to the north and south of center. The presence of these structures at all three wavelengths demonstrates that they are

real features of the source rather than artifacts of the imaging and deconvolution process.

Figure 3 compares our ATCA observations with the *Chandra* data of Park et al. (2002). It can be seen from the lower two panels of this comparison that while all the bright X-ray emission is confined to a circular region well within the radio perimeter of the plateau, there is, as noted by Park et al. (2002), diffuse X-ray emission at larger radii, at a surface brightness ~ 10 times fainter than for the bright interior regions. The bottom panel of Figure 3 shows that this latter component extends right to the edge of the radio plateau around most parts of the SNR, and is similarly sharp- and straight-edged in most places. In the south-eastern quadrant of the SNR, the X-rays at the radio perimeter are much fainter than in the rest of the source, but still extend out to this sharp outer edge. (Note that at its most southerly and western extents, the SNR extends beyond the extent of the *Chandra* ACIS-S CCD, so that we cannot make statements about the outermost extent of the X-rays in these regions.) The arrows in the upper two panels of Figure 3 also indicate that the radio filamentary structures seen to the north and south of the core all have X-ray counterparts in the emission as seen by *Chandra*, a point discussed further in §4.4 below. The analyses of Park et al. (2002) and of Gonzalez & Safi-Harb (2003) demonstrate that these filaments have thermal X-ray spectra.

In Figure 4 we show the central region of hard non-thermal X-rays, corresponding to the PWN identified by Hughes et al. (2001). The upper panel of Figure 4 demonstrates that the brightest regions of the nebula are centrally concentrated, and have a much smaller extent than the core region of the radio source. However, as can be seen in the lower panel, the faintest regions of the X-ray nebula extend to fill a significant fraction of the radio core.

We have formed images of the SNR (not shown here) with the shortest baselines excluded, so as to maximize sensitivity to an embedded point source. Above our $5\text{-}\sigma$ sensitivity level of 2.5 mJy at 20 cm, we find no evidence for a central point source. This is consistent with the 20-cm flux density for PSR J1124–5916 of $80 \mu\text{Jy}$ determined by Camilo et al. (2002).

3.2. Spectral Index Determination

Spectral indices were derived from the images matched in $u-v$ coverage as described in §2. The calculation of spectral indices was carried out through spatial tomography (for discussion and implementation of this approach see Katz-Stone & Rudnick 1997; Crawford et al. 2001; DeLaney et al. 2002). Spatial tomography between two images, I_1 and I_2 , involves scaling I_2 by a trial spectral index α_t (where $I_\nu \propto \nu^\alpha$), and then subtracting this scaled image from I_1 . This then forms a difference image,

$$I_t = I_1 - \left(\frac{\lambda_2}{\lambda_1} \right)^{\alpha_t} I_2, \quad (1)$$

where λ_1 and λ_2 are the observing wavelengths corresponding to I_1 and I_2 respectively. The spectral index, α , of a feature is then the value of α_t at which the emission from this feature blends into the background. An uncertainty in α is determined by finding the range in values of α_t at which the residual at this position in the difference image becomes significant.

The resulting tomography series for 20 cm vs 6 cm data is shown in Figure 5; comparisons between 20/13 cm and 13/6 cm are not shown here, but give similar results. These images clearly demonstrate spatial variations in the spectral index dis-

tribution. We first consider the two main components of emission: the central core and the surrounding plateau. The core clearly has a spectral index $\alpha = -0.05 \pm 0.05$; the mottled appearance of the core in these panels is most likely due to slight differences in the deconvolution process between 20 and 6 cm. The plateau appears to have a spectral index $\alpha = -0.5 \pm 0.1$. This can most clearly be seen along the western rim of the SNR, where positive (black) emission can be seen in the panel corresponding to $\alpha_l = -0.40$, and negative (white) emission can be seen at $\alpha_l = -0.60$.

The smaller-scale structures superimposed on the plateau all have flatter spectra than their surroundings. This can most clearly be seen in the panels $\alpha_l = -0.3$, where emission in many regions is white, but the outer edges of the plateau are still black. Specifically, the filaments running north from the center of the core have $\alpha \approx -0.05$, while that to the south has $\alpha \approx 0$. The prominent spur extending to the south-west of the core has a spectrum $\alpha \approx -0.1$.

3.3. Polarimetry

Linearly polarized emission from SNR G292.0+1.8 is detected in all three wavebands. Significant levels of polarized emission are only seen from the core region, where typical levels of fractional polarization are 1–5% at 20 cm, 5–15% at 13 cm and 10–20% at 6 cm. The distribution of polarized emission in the core at 13 and 6 cm is shown in Figure 6. The morphologies at these two wavelengths are similar, consisting of several bright “fingers” of polarization, with channels of reduced polarization between them. There are no unusual properties of the polarized emission at or near the position of PSR J1124–5916. The 20 cm polarization (not shown here) shows a comparable morphology, but appears to suffer from significant beam and bandwidth depolarization.

In the lower panel of Figure 6 we have plotted the orientation of the magnetic field within the core, assuming this to be oriented perpendicular to the intrinsic position angles of polarization. While the field is well-ordered in small regions, no correlation between orientation and polarized intensity is apparent — in some regions the field runs along the “fingers”, and in other places is perpendicular to them.

It is difficult from these data to put strong constraints on the presence of any polarized emission from the surrounding plateau region. At 20 cm the depolarization effects are severe, at 13 cm the off-axis polarimetric response is very poor, and at 6 cm this region is too faint and extended to be well-imaged. At 13 cm, we roughly estimate an upper limit on the fractional polarization of this region of $\sim 20\%$.

3.4. HI Absorption

In the top panel of Figure 7, we show an HI emission spectrum from a region adjacent to the SNR, taken from the Southern Galactic Plane Survey (McClure-Griffiths et al. 2002). This profile shows at least four peaks in HI emission in this direction, at LSR velocities of approximately -30 , -20 , -8 and 0 km s $^{-1}$. In the lower panel of Figure 7, we show an HI absorption spectrum for the bright core of SNR G292.0+1.8. The SNR shows clear absorption towards all four of the peaks seen in HI emission.

4. DISCUSSION

The nature of the radio morphology of G292.0+1.8 has been uncertain: Lockhart et al. (1977) argued that the whole source was a synchrotron nebula powered by a pulsar, while Braun et al. (1986) developed a model in which G292.0+1.8 had no pulsar-powered component, but rather was a “shell”-type SNR interacting with a molecular cloud. We here discuss our new data on this source, and interpret them in the context of the recent *Chandra* observations and pulsar detection.

4.1. The Distance to G292.0+1.8

The HI absorption profile obtained for SNR G292.0+1.8 by Caswell et al. (1975) showed strong absorption at -30 km s $^{-1}$, with three other possible absorption features seen in the range -30 to 0 km s $^{-1}$ at lower significance. Caswell et al. (1975) interpreted this spectrum as indicating that the SNR was beyond the tangent point in this direction. Using the Galactic rotation curves available at that epoch, they adopted a lower limit on the distance to G292.0+1.8 of 3.7 kpc. However, we note that the most commonly quoted distance in the literature is 4.8 ± 1.6 kpc, which was derived by Saken, Fesen & Shull (1992) using the data of Caswell et al. (1975), but adopting 0 km s $^{-1}$ as an upper limit on the SNR’s systemic velocity. However, such an upper limit can only be established by a clear lack of HI absorption towards an emission feature (e.g. Frail & Weisberg 1990). Since HI emission at 0 km s $^{-1}$ showed a possible counterpart in absorption, no upper limit on the SNR’s distance can be derived from these data.

The absorption towards the SNR shown in Figure 7 confirms that all four absorption lines seen by Caswell et al. (1975) are genuine. A formal lower limit on the SNR distance comes from the fact that HI absorption is seen out to the most negative velocities for which gas is present, representing the tangent point in this direction. Using the best-fit model for Galactic rotation of Fich, Blitz & Stark (1989), and adopting Galactic parameters of $\Theta_0 = 220$ km s $^{-1}$ and $R_0 = 8.5$ kpc (Kerr & Lynden-Bell 1986), we adopt the tangent point distance of 3.2 kpc as a lower limit on the SNR’s distance. (This reconfirms the result of Caswell et al. 1975, who came to the same conclusion but using $R_0 = 10$ kpc.)

A further constraint on the distance can be obtained by a comparison between the HI emission spectrum seen in Figure 7 and the foreground absorption seen in X-rays. For an optically thin HI emission spectrum for which the brightness temperature is T_b at a velocity v , the corresponding hydrogen column density corresponding to the emitting HI in the velocity range $v_1 < v < v_2$ is:

$$N_H = C_H \int_{v_1}^{v_2} T_b dv, \quad (2)$$

where $C_H = 1.823 \times 10^{18}$ cm $^{-2}$. Integrating the HI emission spectrum seen in the top panel of Figure 7 over the velocity range $-100 < v < 0$ km s $^{-1}$, we correspondingly infer a total column density $N_H \approx 3.3 \times 10^{21}$ cm $^{-2}$ for all HI gas along the line-of-sight with negative velocities.⁴ This value agrees well with the column density $N_H = (3-5) \times 10^{21}$ cm $^{-2}$ determined from photoelectric absorption seen in the X-ray spectrum of the SNR G292.0+1.8 (Hughes et al. 2001; Gonzales & Safi-Harb 2003). We thus conclude that all gas at negative velocities is in front of the SNR. Independent evidence for this conclusion is provided by the good match between the SNR’s HI absorption profile and the corresponding HI emission spectrum, which together show four peaks/troughs at matching velocities.

⁴Repeating the integration over the velocity range $0 < v < 200$ km s $^{-1}$, we find a contribution $N_H \sim 1.8 \times 10^{21}$ cm $^{-2}$ for gas at positive velocities.

Considering the Galactic spiral structure in this direction, we find that at distances between ~ 2 and ~ 8 kpc, this line-of-sight runs largely tangent to the Sagittarius-Carina spiral arm, of which the Galactic rotation curve implies that gas out to 6.2 kpc will have negative velocities, and material beyond this point will have positive velocities. We have determined above that the SNR is behind all the negative-velocity gas in this direction. Since it is highly unlikely that this foreground gas is confined to only the near part of the spiral arm, we conclude that the most likely lower limit for the SNR is a systemic velocity of 0 km s^{-1} , corresponding to a distance of at least $6.2 \pm 0.9 \text{ kpc}$.⁵ This is broadly consistent with the distance to the SNR of 5.4 kpc implied by reddening of its optical filaments (Goss et al. 1979), and with the distance of $6.4 \pm 1.3 \text{ kpc}$ implied by the dispersion measure of the associated pulsar J1124–5916 (Cordes & Lazio 2002). In future discussion, we adopt a distance to the system of $6d_6 \text{ kpc}$.

4.2. The Core

The core is centrally brightened, significantly polarized, has a flat spectrum, and contains the young pulsar J1124–5916. By analogy with the many other sources known to have such properties (see Gaensler 2001), we interpret the radio core as a PWN powered by PSR J1124–5916.

The effects of Faraday rotation, both interior to the source and in the foreground, can produce complicated structures in polarization (Gaensler et al. 2001). However, the morphology and intensity of such structures show a very strong wavelength dependence. In contrast, the structure of the polarized intensity in the core of G292.0+1.8 shows little difference between 6 and 13 cm, which implies that Faraday effects are negligible, and that the observed distribution of linear polarization is intrinsic to the source. In this case, we interpret the fingers of bright polarization as representing regions of well-ordered magnetic field, and the linear channels of reduced polarization as resulting from beam depolarization, where the intrinsic orientation of magnetic field changes on scales much smaller than the resolution limit. These results demonstrate a complicated and tangled geometry for the nebular magnetic field in some regions, in contrast to the well-ordered field structure seen over the entire extent of the Crab Nebula (Hickson & van den Bergh 1990; Hester et al. 1995). In §4.3 below, we argue that the PWN is in the early stages of an interaction with the SNR reverse shock; it is possible that this process might produce this complicated magnetic field geometry.

At 20 cm the PWN has a flux density of 5.5 Jy and a spectral index $\alpha \approx -0.05$, while at 1 keV, its flux density is $\sim 2\text{--}4 \mu\text{Jy}$ and the spectral index is $-1.1 \lesssim \alpha \lesssim -0.7$ (Hughes et al. 2001). Extrapolating between these two data-points, we find that a break in the spectrum $\Delta\alpha \sim 1$ is inferred at a frequency $\nu_b \lesssim 800 \text{ GHz}$. If we interpret such a break as being due to synchrotron cooling, then the age of the source allows us to compute the nebular magnetic field (e.g. Gaensler et al. 2002).

The exact age of SNR G292.0+1.8 is unclear: model dependent analyses of the optical and X-ray spectra emission from this source suggest ages of $t = 2000d_6 \text{ yr}$ (Murdin & Clark 1979; Braun et al. 1983) and $t = 2600 \text{ yr}$ (Gonzales & Safi-Harb 2003) respectively, while the pulsar’s characteristic age is $\tau_c \equiv P/2\dot{P} = 2900 \text{ yr}$ (Camilo et al. 2002). If in subsequent discussion we adopt an age $t = 2500t_1 \text{ yr}$, the implied nebular

magnetic field is $B_n \gtrsim 410t_1^{-2/3} \mu\text{G}$ (e.g. Frail et al. 1996). Such a large magnetic field is difficult to explain, as the resulting synchrotron lifetime in X-rays would then be only $\sim 5 \text{ yrs}$, which is inconsistent with the observed large extent of the X-ray PWN. A nebular magnetic field $B_n \sim 3 \mu\text{G}$, as inferred from the radius of the termination shock surrounding the pulsar, seems more likely (Hughes & Slane 2003). We therefore think it likely that the implied break in the nebular spectrum is not simply due to synchrotron losses.

A second possibility to account for the broad-band spectrum is that the radio and X-ray emission in this source originate from entirely distinct populations, and that to extrapolate between the flux densities of the two regimes is not meaningful. Indeed in the Crab Nebula, models cannot simultaneously account for both the radio and high-energy emission from the same particle population (Kennel & Coroniti 1984).

Alternatively, for a single emitting population, a PWN spectrum with just one synchrotron break only occurs if the pulsar’s rate of energy output has been approximately constant over its lifetime (Pacini & Salvati 1973; Reynolds & Chevalier 1984). This is a valid assumption only at times $t < \tau_0 \equiv 2\tau_c/(n-1) - t_p$, where t_p is the pulsar’s true age, and $\tau_c \equiv P/2\dot{P}$ is its characteristic age (Pacini & Salvati 1973). However, for times $t > \tau_0$ (“phase 3” of Pacini & Salvati 1973), the spin-down luminosity of the pulsar is substantially reduced, and the emission from the PWN effectively has contributions from two different populations of particles. There can thus be multiple spectral breaks in the PWN spectrum, and the simple arguments made above then do not apply. In the case of PSR J1124–5916, we have that $\tau_c = 2900 \text{ yrs}$ and $t_p = 2500t_1 \text{ yr}$. Requiring that $t_p > \tau_0$, we find that $n > \tau_c/t_p + 1 \gtrsim 2.2$. While the braking index has not yet been measured for this pulsar, it is certainly reasonable that it falls in this range (e.g. Manchester, Durbin, & Newton 1985; Camilo et al. 2000), in which case multiple breaks would indeed be expected in the nebular spectrum.

Finally, it is important to note that a variety of PWNe have been shown to have a single steep spectral break, $\Delta\alpha > 0.5$, at a relatively low frequency, $\nu_b \lesssim 100 \text{ GHz}$. The nature of these low-frequency breaks is not understood (Green & Scheuer 1992; Woltjer et al. 1997). It has been speculated that they result from the anomalous properties of the central pulsar, but the recent detection of the apparently Crab-like young pulsar J0205+6449 in the prototypical low-frequency-break PWN 3C 58 (Murray et al. 2002) suggests that some other effect is at work. The PWN powered by PSR J1124–5916 could similarly show such properties, and this could also explain its X-ray and radio flux densities.

The PWN in SNR G292.0+1.8 is notable in that, as shown in Figure 4, its overall radio and X-ray extents are similar. This is contrary to the situation seen in the Crab Nebula, where the X-ray nebula is much smaller than that seen in the radio, reflecting the much shorter synchrotron lifetimes of X-ray emitting particles. However, in this case the very low nebular magnetic field, $B_n \sim 3 \mu\text{G}$ (Hughes & Slane 2003), implies a synchrotron lifetime in the X-ray band larger than the age of the system. X-ray emitting electrons can thus flow out to largely fill the volume delineated by the radio PWN, resulting in little change of the nebular extent with observing wavelength. A similar situation is seen for the PWN powered by PSR B1509–58, which also has a low nebular magnetic field and hence a large X-ray extent

⁵The error quoted in the distance incorporates both a 10% uncertainty in comparing N_H from Equation (2) with that from X-rays, and a typical uncertainty of $\pm 7 \text{ km s}^{-1}$ in converting systemic velocities to distances due to the random motions of HI clouds.

(Gaensler et al. 2002).

4.3. The Plateau

The plateau region is morphologically and spectrally distinct from the core. However, it could be argued that this outer component is also powered by the pulsar. In this case, the steeper spectrum of this region could be due to synchrotron losses in particles which have traveled further from the pulsar, as is seen in X-rays for several other PWNe (Slane et al. 2000; Bocchino et al. 2001). However, in such a case one would expect the PWN to steadily fade and steepen in its spectrum with increasing radius due to synchrotron losses, at odds with the sharp transition in surface brightness and spectral index seen here. Furthermore, for synchrotron cooling to be efficient at radio frequencies, the nebular magnetic field would have to be even higher than the problematic value considered in §4.2 above.

Given that the X-ray PWN coincides with the radio PWN, but that thermal X-ray emission extends over most of the radio plateau region, we therefore interpret the plateau as corresponding to the standard “shell” component of the SNR, representing the supernova shock and its interaction with its environment. Given this interpretation, G292.0+1.8 clearly can be classified as a “composite” SNR, showing a characteristic flat-spectrum core surrounded by a steep-spectrum shell (e.g. Helfand & Becker 1987). In this sense, G292.0+1.8, along with G11.2–0.3, Kes 75 and 0540–69.3, is one of a handful of “text-book” SNRs which show a central young pulsar, its associated X-ray/radio synchrotron nebula, and an enveloping SNR shell.

Figure 2 demonstrates that the plateau shows a sharp outer edge, while the lower panel of Figure 3 shows that this edge also corresponds in most places to a faint and similarly sharp-edged perimeter of X-ray emission. Several other young SNRs are sharp-rimmed in both radio and X-rays, most notably SN 1006, Tycho’s SNR and Cas A (Reynolds & Gilmore 1986; Dickel, van Breugel, & Strom 1991; Gotthelf et al. 2001; Hwang et al. 2002). This morphology is thought to indicate that diffusive shock acceleration is occurring at the outer edge of the SNR — the sharpness of the edge is due to enhanced turbulence ahead of the SNR blast wave, which prevents synchrotron-emitting electrons from diffusing upstream (Achterberg, Blandford, & Reynolds 1994). Thus, as for other sharp-rimmed SNRs, we identify this outer radio and X-ray edge as corresponding to the forward shock of the SNR, where ambient gas is first shocked by the remnant. The radius of this shock is $4'$, corresponding to a shock radius $R = 7.0d_6$ pc. At least in the case of SN 1006, the sharp outer edge of X-ray emission has been shown to be non-thermal, corresponding to electrons which have been accelerated by the shock up to TeV energies. In the case of SNR G292.0+1.8, the available data suggest a thermal spectrum for this outermost rim (Park et al. 2002; Gonzales & Safi-Harb 2003). However, this region is very faint, and deeper X-ray observations will be needed to constrain the presence of any non-thermal component. Park et al. (2002) identify a continuous ring of X-ray filaments $1' - 2'$ interior to this outer edge, and propose that it corresponds either to the SNR forward shock or to circumstellar material overrun by the shock. Clearly the fact that both radio and X-ray emission from the SNR extend beyond this filamentary ring favors the latter alternative.

The identification of a complete outer rim representing the forward shock allows us to estimate the position of the SNR’s geometric center. We fit a circle to this outer rim, and find a best-fit center of (J2000) RA $11^{\text{h}}24^{\text{m}}34.^{\text{s}}8$, Dec $-59^{\circ}15'52''.9$, with an uncertainty of $\pm 5''$ in each coordinate. The position of

PSR J1124–5916 as determined by Hughes et al. (2001) is offset from this position by $\approx 45''$. If the SNR’s geometric center coincides with the explosion site, we can infer a projected pulsar velocity for PSR J1124–5916 of $520d_6/t_1$ km s^{-1} , which is typical of the velocity distribution seen for the Galactic pulsar population (Arzoumanian, Chernoff, & Cordes 2002). Despite this high pulsar velocity, the PWN does not have a bow-shock morphology because its motion is currently not supersonic in the gas in the SNR’s interior (van der Swaluw, Achterberg, & Gallant 1998).

An important difference between G292.0+1.8 and the vast majority of other SNRs is that most SNRs show significant limb-brightening, with little interior radio emission other than that corresponding to an associated PWN. This appearance is thought to correspond to a thin spherical shell of synchrotron emission, which we only see around the edges because of projection effects. However, in the case of G292.0+1.8, little or no limb-brightening is seen around the perimeter of the plateau, except perhaps along the south-western edge. Rather, the plateau region of G292.0+1.8 appears as a very thick annulus, with a ratio of outer radius to inner radius of ~ 2 .

Once an expanding SNR has swept up a significant amount of mass from the ambient medium, it enters the “Sedov-Taylor” phase of evolution during which it takes on a structure consisting of both the forward blast wave and a reverse shock interacting with supernova ejecta. We expect radio emission to be produced not just at the outer blast wave, but also through turbulence and particle acceleration in relativistic material between the two shocks (e.g. Jun & Jones 1999). Thus the interpretation we propose for the thickness of the plateau region is that SNR G292.0+1.8 is in a moderately evolved state, in which the forward and reverse shocks are at markedly different radii, and in which radio emission fills the region between them. Well-separated forward and reverse shocks with a thick radio plateau between them have been clearly identified in Cas A (Anderson et al. 1991; Gotthelf et al. 2001), while thick radio shells as seen here have been similarly interpreted in SNRs Kes 79 (G33.6+0.1) and DA 495 (G65.7+1.2) (Velusamy et al. 1989; Velusamy, Becker, & Seward 1991). Indeed, from earlier radio data on G292.0+1.8 in which the plateau and core regions were not identified as being spectrally distinct, Braun et al. (1986) interpreted the entirety of G292.0+1.8 as corresponding to part of such a thick shell.

Truelove & McKee (1999, hereafter TM99) present detailed models for the evolution of a SNR and its shock structure. The exact positions of the forward and reverse shocks depend on the density distributions of the ejecta and of the ambient medium, but for a wide variety of such possibilities, TM99 show that a ratio of forward shock to reverse shock radius of ~ 2 typically occurs after a time $t \sim 1.4t_{ch}$, at which point the radius of the forward shock is $R \sim 1.25R_{ch}$ and its velocity is $V \sim 0.4V_{ch}$, where t_{ch} and R_{ch} are characteristic time and size scales for the system, respectively, and $V_{ch} = R_{ch}/t_{ch}$. Since $R = 7.0d_6$ pc and $t = 2500t_1$ yr, we can thus infer that $R_{ch} \approx 5.6d_6$ pc, $t_{ch} \approx 1800t_1$ yr and $V_{ch} = 3100d_6/t_1$ km s^{-1} . The latter implies that $V \sim 0.4V_{ch} \approx 1200d_6/t_1$ km s^{-1} which is broadly consistent with the expansion velocity inferred from optical spectroscopy (Braun et al. 1983). These filaments are coincident with the PWN in projection, but are presumably physically located near the front or back of the SNR. The rate of expansion implied by the inferred velocity is $43/t_1$ mas yr^{-1} , which should be detectable with both *Chandra* and the ATCA in another ~ 5 years.

Assuming that the medium into which the SNR expands is homogeneous, Table 2 of TM99 gives that:

$$R_{ch} = 3.07 M_{ej}^{1/3} n_0^{-1/3} \text{ pc} \quad (3)$$

and

$$t_{ch} = 423 E_{51}^{-1/2} M_{ej}^{5/6} n_0^{-1/3} \text{ yrs}, \quad (4)$$

where $M_{ej} M_{\odot}$ is the mass of the supernova ejecta, $n_0 \text{ cm}^{-3}$ is the atomic density of the ambient medium and $E_{SN} = E_{51} \times 10^{51} \text{ erg}$ is the kinetic energy of the supernova explosion. With these definitions, it can be shown that the ratio of swept-up mass, M_{sw} , to ejected mass is $X \equiv M_{sw}/M_{ej} \approx 3.0(R/R_{ch})^3$. Thus in the case of G292.0+1.8, independently of distance we can infer $X \sim 6$. Solving Equations (3) and (4) simultaneously to eliminate M_{ej} and n_0 respectively, we find that:

$$n_0 = 0.9 d_6^{-5} t_1^2 E_{51} \text{ cm}^{-3} \quad (5)$$

and

$$M_{ej} = 5.4 d_6^{-2} t_1^2 E_{51} M_{\odot}. \quad (6)$$

Braun et al. (1986) interpret the infrared emission from the SNR as resulting from shock-heated dust. Re-arranging their Equation (4), one obtains:

$$n_0 = 0.7 \left(\frac{V}{1000 \text{ km s}^{-1}} \right)^{-5/3} \left(\frac{\lambda_{peak}}{40 \mu\text{m}} \right)^{-50/9} \text{ cm}^{-3}, \quad (7)$$

where λ_{peak} is the peak wavelength of infrared emission. Braun et al. (1986) determine $\lambda_{peak} = 36 \pm 1 \mu\text{m}$; Saken, Fesen & Shull (1992) obtain the same value in their analysis. For $V = 1200 d_6/t_1 \text{ km s}^{-1}$ as determined above, Equation (7) then yields $n_0 \approx 0.9 d_6^{-5/3} t_1^{5/3} \text{ cm}^{-3}$. Substituting this density into of this value into Equations (5) and (6), we find that $E_{SN} \approx 1.1 d_6^{10/3} t_1^{-1/3} \times 10^{51} \text{ erg}$ and $M_{ej} \approx 5.9 d_6^{4/3} t_1^{5/3} M_{\odot}$, both typical values for a core-collapse SNR.

An important point to note is that the above calculations assume that the reverse shock progresses steadily through supernova ejecta. This is a reasonable assumption in the case of a shell SNR, but the presence of a central PWN complicates the situation — the expanding PWN will eventually collide with the reverse shock, causing a complicated intermediate phase in the system's evolution (Reynolds & Chevalier 1984; Chevalier 1998). Specifically, the boundary between the SNR reverse shock and the PWN's forward shock will reverberate back and forth until pressure balance is established, crushing the PWN in the process (van der Swaluw et al. 2001; Blondin, Chevalier, & Frierson 2001). Clearly if the reverse shock's position has been substantially affected by this process, its position can then not be compared to that in standard SNR evolution models. The fact that there is no obvious gap between the inner boundary of the plateau and the outer regions of the core suggests that the reverse shock and the PWN may have indeed already collided and interacted.

However, in this case we think it likely that the reverse shock has only recently begun interacting with the PWN, and that the SNR evolution has not yet been significantly affected by this process. Our main argument for this is simply that the PWN radius is larger than would be expected during this interaction process. Equation (5) of Blondin et al. (2001) provides the radius of the PWN, R_p , as a function of time before it collides with the SNR reverse shock. For the parameters corresponding to G292.0+1.8 and PSR J1124–5916, the model of Blondin

et al. (2001) predicts $R_p \sim 3 \text{ pc}$, in approximate agreement with the value $R_p \approx 3.5 d_6 \text{ pc}$ observed for the radio core. However, during the subsequent interaction process, the PWN is typically 2–5 times smaller than this (van der Swaluw et al. 2001; Blondin, Chevalier, & Frierson 2001). At later times, when pressure balance has been established, the PWN then expands steadily again. However, in this stage the compression of the nebula results in a small X-ray PWN centered on the pulsar, substantially offset from a larger radio PWN with an irregular morphology (Chevalier 1998; Blondin, Chevalier, & Frierson 2001). This is not observed in the case of G292.0+1.8, for which Figures 1 and 4 demonstrate the radio morphology to be broadly circular, the pulsar to be centrally located, and the radio and X-ray emission from the PWN to roughly correspond. In summary, we conclude that in this case the reverse shock is only now beginning to interact with the PWN, and that the SNR evolution model of TM99 can still be validly applied.

4.4. Flat Spectrum Filaments

We demonstrated in §3.2 that many of the filamentary structures in the plateau region have flat spectra, $-0.1 \leq \alpha \leq 0$, in contrast to the steeper spectrum for the diffuse plateau emission, $\alpha = -0.50$. Since these filaments all have counterparts seen in thermal X-ray emission with *Chandra*, we can thus rule out that these flat-spectrum structures are part of the PWN. It rather appears that there are two discrete contributions to the shell component of the SNR, the plateau and the filaments, distinguished by their distinct spectral indices.

While significant variations in spectral index have been seen for many other shell SNRs (see Anderson & Rudnick 1993 for a review), what is striking here is the clear morphological separation between the steep-spectrum diffuse emission, and the flat-spectrum filaments. Only in a few other SNRs, most notably Cas A and the Cygnus Loop, is there such a clear correlation between the structure of emitting features and their spectral indices (Anderson & Rudnick 1996; Leahy & Roger 1998).

It is not easy to produce the flat spectral index seen for the filaments via the same diffuse shock acceleration process as we have claimed is operating for the steeper spectrum plateau. For an adiabatic shock in the test-particle approximation, the maximum compression ratio is 4, and the corresponding synchrotron spectral index of accelerated particles will be no flatter than $\alpha = -0.5$. Non-linear processes such as the escape of high energy particles from the shock, the presence of relativistic particles with their softer equation-of-state, and the smoothing of the shock via the back-pressure of accelerated particles can all serve to result in higher effective compression ratios and thus flatter emergent synchrotron spectra. However, when these effects are considered in detail, the resultant spectral index is no flatter than $\alpha = -0.25$ (Ellison & Reynolds 1991; Berezhko & Ellison 1999), which is insufficient to explain the still flatter values seen here.

Another way in which a spectral index flatter than $\alpha = -0.5$ can be produced via diffuse shock acceleration is if the particle population encounters and is accelerated by multiple shocks. While a completely flat spectrum, $\alpha = 0$, can only be achieved in the limit of an infinite number of shocks (Melrose & Pope 1993 and references therein), only ~ 5 successive shocks are needed to produce spectra as flat as $\alpha \approx -0.1$ (Gieseler & Jones 2000). The turbulent and unstable nature of the gas flow between the forward and reverse shocks (e.g. Jun & Norman 1996a,b) may indeed present the opportunity for particles to be shocked and

accelerated on multiple occasions. However, it is difficult to see in such a situation how the flat-spectrum regions could be maintained only in discrete filamentary structures, morphologically distinct from steeper surrounding diffuse emission. We thus regard this possibility also as unlikely.

de Jager & Mastichiadis (1997) have proposed that in the case of SNR W44, flat-spectrum emission in the shell is produced via electron injection into the shell by the associated pulsar PSR B1853+01. Applying equipartition energy arguments to the synchrotron emission from the plateau component of G292.0+1.8 (Pacholczyk 1970), we find for this region $E_{min} \approx 5 \times 10^{48}$ erg. The energy lost by PSR J1124–5916 since birth is $\frac{1}{2}I(\omega_0^2 - \omega^2)$, where $I \equiv 10^{45}$ g cm², $\omega = 2\pi/P \approx 47$ s⁻¹, and ω_0 is the initial value of ω . For sufficiently rapid initial periods ($P_0 = 2\pi/\omega_0 \lesssim 20$ ms), it is energetically feasible for the pulsar to have both powered its PWN (which has an internal energy $E_{PWN} \approx 4 \times 10^{49}$ erg; Hughes & Slane 2003) and have provided significant energy to the plateau region as well. However, while we cannot completely rule out some level of mixing between particles in the PWN and the shell, particularly once the reverse-shock interaction discussed in §4.3 begins, it seems unlikely that this process would occur only in the select regions corresponding to the flat-spectrum filaments, particularly given the broadly circular appearance of the PWN.

Leahy & Roger (1998) identify a collection of flat-spectrum filaments in the Cygnus Loop, potentially similar to the structures seen here for G292.0+1.8. Leahy & Roger (1998) argue that in their case, this flattening is caused by free-free absorption by thermal material within the filaments. Since the flat-spectrum structures seen in G292.0+1.8 coincide with X-ray emitting filaments, we can use the X-ray properties of this source to estimate whether such an effect is likely to be operating here. Gonzalez & Safi-Harb (2003) have carried out spectral fits to a variety of regions within the SNR using high-resolution *Chandra* data. The flat-spectrum radio filaments correspond to their regions 16, 17 and 18, for which the X-ray spectra imply electron temperatures $T_e \approx 1 \times 10^7$ K and volume emission measures $n_e^2 V_e \approx 3d_6^2 \times 10^{56}$ cm⁻³ (Safi-Harb, private communication, 2003), where n_e is the electron density of emitting material, and V_e is the emitting volume. Assuming a depth comparable to their extent on the sky, the emitting volumes of each of these regions is $V_e \sim 2d_6^3 \times 10^{55}$, so that $n_e \sim 4d_6^{-1/2}$ cm⁻². For the inferred values of T_e and n_e the resulting optical depth for free-free absorption is completely negligible, and this effect is thus not likely to be operating here.

An intriguing possibility is that the flat- and steep-spectrum components represent two distinct mechanisms for particle acceleration. It seems clear from the discussion in §4.3 above that diffuse shock acceleration is occurring at the outer edge of the radio SNR, to which the plateau emission with $\alpha = -0.5$ can be attributed. However, synchrotron emission in SNRs may also result from either simple compression of an ambient population of relativistic particles (van der Laan 1962), or from stochastic (second-order Fermi) particle acceleration in shocked gas (Cowsik & Sarkar 1984). We consider in turn whether either of these mechanisms could be taking place here and could produce the flat-spectrum filaments.

Very high compression ratios can be achieved in radiative shocks. In such cases, the ambient electron cosmic ray population can be compressed to produce bright synchrotron emission, with a spectrum distinct from that of the particle population accelerated by the shock. Longair (1997, p. 284) demon-

strates that the synchrotron spectrum produced by cosmic ray electrons can be as flat as $\alpha = -0.3$ for electrons with energies < 100 MeV. However, to cause such particles to radiate at ~ 5 GHz requires an extreme compression of $> 10^4$, and cannot produce a sufficiently flat spectrum to match our observations in any case.

Finally, we consider the possibility that second-order Fermi acceleration could be operating in these filaments. The diffusion in momentum space resulting from this process can flatten the particle spectrum, and can result in synchrotron spectra as flat as $\alpha \approx -0.1$ as required here (Schlickeiser & Fürst 1989; Ostrowski 1999). Such effects can only dominate when $\beta \equiv P_{th}/P_{mag} \lesssim 0.05$, where P_{th} and P_{mag} are the thermal and magnetic pressure in the gas, respectively (Schlickeiser & Fürst 1989). The density and temperature in the filaments, inferred above from the X-ray analysis of Gonzalez & Safi-Harb (2003), imply a thermal pressure $P_{th} \approx 5 \times 10^{-9}$ erg cm⁻³. For $\beta \lesssim 0.05$ we thus require $P_{mag} \gtrsim 1 \times 10^{-7}$ erg cm⁻³ and hence a magnetic field in the filaments $B \gtrsim 1$ mG. For a typical ambient ISM magnetic field strength of ~ 3 μ G, compression by a strong shock should produce a magnetic field in the emitting regions of only 12 μ G. However, Jun & Norman (1996b) have demonstrated that this magnetic field can be strongly amplified around the edges of elongated “fingers” produced by Rayleigh-Taylor instabilities at the contact discontinuity between the forward and reverse shocks. In their two-dimensional simulations, these authors find a magnetic field amplification by up to a factor of 60 over ambient values. Jun & Norman (1996b) argue that in three dimensions and at higher resolutions, much higher field amplifications are likely to result (see also Jun & Norman 1996a). We thus argue that magnetic fields as strong as required here can indeed be produced in SNRs, and that they specifically should result in elongated radial structures lying between the forward and reverse shocks. We therefore interpret the flat-spectrum filaments seen in G292.0+1.8 as Rayleigh-Taylor instabilities at the contact discontinuity between ejected and ambient material in the shock, where amplification has produced high magnetic fields and hence efficient second-order Fermi acceleration. This process produces the flat spectral index seen in the filaments.

In comparison to the other possibilities considered above, this interpretation alone can account for the very flat spectra seen only in these distinct, elongated filaments. The key to confirming this interpretation lies in the identification of linearly polarized emission from these regions, which we predict to be a significant fraction of the total and to have a radially aligned underlying magnetic field orientation. Sensitive polarimetric observations of the plateau region will be needed to investigate this possibility.

5. CONCLUSIONS

We have presented a detailed multi-frequency radio study of the young oxygen-rich SNR G292.0+1.8 and its pulsar wind nebula. We find that the SNR morphology is composed of three main components: a central core, a surrounding plateau, and a set of radial filaments superimposed on the plateau.

The core is polarized, filled-center, has a flat radio spectrum ($\alpha = -0.05 \pm 0.05$) and is coincident with PSR J1124–5916. We conclude that this source represents radio emission produced by the PWN powered by the pulsar. Comparison of the radio and X-ray spectra for this source indicates that there must be a spectral break between the two bands; this steepening cannot be accounted for by synchrotron losses. The high surface brightness

of the core allows us to measure H I absorption in this direction at high signal-to-noise. This spectrum shows absorption out to the tangent point along this line-of-sight, implying a lower limit on the SNR distance of 3.2 kpc. Comparison of the hydrogen absorbing column implied by X-ray and H I observations in this direction, along with the shape of the H I absorption profile seen towards the SNR, argue that the SNR is behind all H I within the solar circle, implying a more likely minimum distance of 6 kpc to the system.

We interpret the steep-spectrum ($\alpha = -0.5 \pm 0.1$) plateau which surrounds the core as corresponding to the SNR shell. The plateau shows a sharp outer edge in both radio and X-rays, indicating the presence of diffusive shock acceleration at the forward shock. The thickness of the plateau indicates that the SNR reverse shock is at a much smaller radius, having significantly progressed back towards the center of the SNR in the reference frame of the outwardly expanding ejecta. The relative positions of the forward and reverse shocks allow us to infer a shock velocity $\sim 1200 \text{ km s}^{-1}$, an ambient density $\sim 0.9 \text{ cm}^{-3}$, an initial explosion energy $\sim 1.1 \times 10^{51} \text{ erg}$ and an ejected mass $\sim 5.9 M_{\odot}$, assuming a distance to the source of 6 kpc and an age of 2500 yr. The inferred location of the reverse shock suggests that this region is beginning to interact with the PWN, but the morphology of the PWN indicates that this process is yet to significantly affect the evolution of the system.

Finally, we identify elongated radial filaments superimposed on the plateau, with a much flatter spectrum ($-0.1 \lesssim \alpha \lesssim 0$) than the surrounding steep-spectrum shell. We consider a number of possible mechanisms for this flat-spectrum emission, and conclude that the most likely explanation is that these filaments represent Rayleigh-Taylor instabilities near the SNR contact dis-

continuity, where the magnetic field is greatly enhanced and hence efficient second-order Fermi acceleration can occur.

These new radio observations, combined with the recent *Chandra* imaging of this source and the subsequent detection of a young radio and X-ray pulsar, result in a consistent picture in which SNR G292.0+1.8 is a moderately evolved SNR, resulting from the core-collapse of a massive progenitor. However, G292.0+1.8 is clearly an unusual and complicated system in many respects. The thick shell with a sharp outer edge, flat-spectrum filaments, and coincidence between the positions of the reverse shock and outer boundary of the PWN are all phenomena seen in few other SNRs, and certainly not all in the same source. Clearly SNR G292.0+1.8 is at a special point in its evolution, only seen at an age of $\sim 2000\text{--}3000 \text{ yr}$, and only for systems containing both bright SNR shells and energetic pulsars. Considering the known population of young pulsars in SNRs (e.g. Kaspi & Helfand 2002), it is clear that only SNR G292.0+1.8 and PSR J1124–5916 meet these requirements. We now look forward to forthcoming detailed spectroscopic studies of this source with *Chandra* and *XMM*, the results from which will be able to better constrain the evolutionary state of and conditions within this remarkable SNR.

We thank Larry Rudnick, Pat Slane, Jack Hughes and Tracey DeLaney for a series of very helpful discussions, and Samar Safi-Harb for supplying information on her spectral fits. We acknowledge the efforts of Grant Gussie in carrying out the original observations for this project. The Australia Telescope is funded by the Commonwealth of Australia for operation as a National Facility managed by CSIRO.

REFERENCES

- Achterberg, A., Blandford, R. D., & Reynolds, S. P. 1994, *A&A*, 281, 220.
 Anderson, M., Rudnick, L., Leppik, P., Perley, R., & Braun, R. 1991, *ApJ*, 373, 146.
 Anderson, M. C. & Rudnick, L. 1993, *ApJ*, 408, 514.
 Anderson, M. C. & Rudnick, L. 1996, *ApJ*, 456, 234.
 Arzoumanian, Z., Chernoff, D. F., & Cordes, J. M. 2002, *ApJ*, 568, 289.
 Berezhko, E. G. & Ellison, D. C. 1999, *ApJ*, 526, 385.
 Blondin, J. M., Chevalier, R. A., & Frierson, D. M. 2001, *ApJ*, 563, 806.
 Bocchino, F., Warwick, R. S., Marty, P., Lumb, D., Becker, W., & Pigot, C. 2001, *A&A*, 369, 1078.
 Braun, R., Goss, W. M., Caswell, J. L., & Roger, R. S. 1986, *A&A*, 162, 259.
 Braun, R., Goss, W. M., Danziger, I. J., & Boksenberg, A. 1983, in *Supernova Remnants and Their X-Ray Emission* (IAU Symposium 101), ed. J. Danziger & P. Gorenstein, (Dordrecht: Reidel), p. 159.
 Camilo, F., Kaspi, V. M., Lyne, A. G., Manchester, R. N., Bell, J. F., D'Amico, N., McKay, N. P. F., & Crawford, F. 2000, *ApJ*, 541, 367.
 Camilo, F., Manchester, R. N., Gaensler, B. M., Lorimer, D. L., & Sarkissian, J. 2002, *ApJ*, 567, L71.
 Caswell, J. L., Murray, J. D., Roger, R. S., Cole, D. J., & Cooke, D. J. 1975, *A&A*, 45, 239.
 Chevalier, R. A. 1998, *Mem. della Soc. Ast. It.*, 69, 977.
 Clark, D. H., Tuohy, I. R., & Becker, R. H. 1980, *MNRAS*, 193, 129.
 Cordes, J. M. & Lazio, T. J. W. 2002, *ApJ*, . submitted, <http://xxx.lanl.gov/abs/astro-ph/0007310>.
 Cowsik, R. & Sarkar, S. 1984, *MNRAS*, 207, 745.
 Crawford, F., Gaensler, B. M., Kaspi, V. M., Manchester, R. N., Camilo, F., Lyne, A. G., & Pivovarov, M. J. 2001, *ApJ*, 554, 152.
 de Jager, O. C. & Mastichiadis, A. 1997, *ApJ*, 482, 874.
 DeLaney, T. and Koralesky, B., Rudnick, L., & Dickel, J. R. 2002, *ApJ*, 580, 914.
 Dickel, J. R., van Breugel, W. J. M., & Strom, R. G. 1991, *AJ*, 101, 2151.
 Dickey, J. M. 1997, *ApJ*, 488, 258.
 Ekers, R. D. & Rots, A. H. 1979, in *Image Formation from Coherence Functions in Astronomy*, ed. C. van Schooneveld, (Dordrecht: Reidel), p. 61.
 Ellison, D. C. & Reynolds, S. P. 1991, *ApJ*, 382, 242.
 Fich, M., Blitz, L., & Stark, A. A. 1989, *ApJ*, 342, 272.
 Frail, D. A., Giacani, E. B., Goss, W. M., & Dubner, G. 1996, *ApJ*, 464, L165.
 Frail, D. A. & Weisberg, J. M. 1990, *AJ*, 100, 743.
 Frater, R. H., Brooks, J. W., & Whiteoak, J. B. 1992, *J. Electr. Electron. Eng. Aust.*, 12, 103.
 Gaensler, B. M. 2001, in *Young Supernova Remnants* (AIP Conference Proceedings Volume 565), ed. S. S. Holt & U. Hwang, (New York: AIP), p. 295.
 Gaensler, B. M., Arons, J., Kaspi, V. M., Pivovarov, M. J., Kawai, N., & Tamura, K. 2002, *ApJ*, 569, 878.
 Gaensler, B. M., Brazier, K. T. S., Manchester, R. N., Johnston, S., & Green, A. J. 1999, *MNRAS*, 305, 724.
 Gaensler, B. M., Dickey, J. M., McClure-Griffiths, N. M., Green, A. J., Wieringa, M. H., & Haynes, R. F. 2001, *ApJ*, 549, 959.
 Gaensler, B. M., Manchester, R. N., & Green, A. J. 1998, *MNRAS*, 296, 813.
 Gieseler, U. D. J. & Jones, T. W. 2000, *A&A*, 357, 1133.
 Gonzales, M. & Safi-Harb, S. 2003, *ApJ*, 583, L91.
 Goss, W. M., Shaver, P. A., Zealey, W. J., Murdin, P., & Clark, D. H. 1979, *MNRAS*, 188, 357.
 Gotthelf, E. V., Koralesky, B., Rudnick, L., Jones, T. W., Hwang, U., & Petre, R. 2001, *ApJ*, 552, L39.
 Green, D. A. & Scheuer, P. A. G. 1992, *MNRAS*, 258, 833.
 Helfand, D. J. & Becker, R. H. 1987, *ApJ*, 314, 203.
 Hester, J. J. et al. 1995, *ApJ*, 448, 240.
 Hickson, P. & van den Bergh, S. 1990, *ApJ*, 365, 224.
 Hughes, J. P. & Singh, K. P. 1994, *ApJ*, 422, 126.
 Hughes, J. P. & Slane, P. O. 2003, *ApJ*, . submitted.
 Hughes, J. P., Slane, P. O., Burrows, D. N., Garmire, G., Nousek, J. A., Olbert, C. M., & Keohane, J. W. 2001, *ApJ*, 559, L153.
 Hwang, U., Decourchelle, A., Holt, S. S., & Petre, R. 2002, *ApJ*, 581, 1101.
 Jun, B.-I. & Jones, T. W. 1999, *ApJ*, 511, 774.
 Jun, B.-I. & Norman, M. L. 1996a, *ApJ*, 472, 245.
 Jun, B.-I. & Norman, M. L. 1996b, *ApJ*, 465, 800.
 Kaspi, V. M. & Helfand, D. J. 2002, in *Neutron Stars in Supernova Remnants*, ed. P. O. Slane & B. M. Gaensler, (San Francisco: Astronomical Society of the Pacific), 3.
 Katz-Stone, D. M. & Rudnick, L. 1997, *ApJ*, 488, 146.
 Kennel, C. F. & Coroniti, F. V. 1984, *ApJ*, 283, 710.
 Kerr, F. J. & Lynden-Bell, D. 1986, *MNRAS*, 221, 1023.
 Leahy, D. A. & Roger, R. S. 1998, *ApJ*, 505, 784.
 Lockhart, I. A., Goss, W. M., Caswell, J. L., & McAdam, W. B. 1977, *MNRAS*, 179, 147.
 Longair, M. S. 1997, *High Energy Astrophysics, Volume 2* (2nd Edition), (Cambridge: Cambridge University Press).
 Manchester, R. N., Durdin, J. M., & Newton, L. M. 1985, *Nature*, 313, 374.

- McClure-Griffiths, N. M., Dickey, J. M., Gaensler, B. M., & Green, A. J. 2002, *ApJ*, 578, 176.
- McClure-Griffiths, N. M., Green, A. J., Dickey, J. M., Gaensler, B. M., Haynes, R. F., & Wieringa, M. H. 2001, *ApJ*, 551, 394.
- Melrose, D. B. & Pope, M. H. 1993, *Proc. Astr. Soc. Aust.*, 10, 222.
- Mills, B. Y., Slee, O. B., & Hill, E. R. 1961, *Aust. J. Phys.*, 14, 497.
- Milne, D. K. 1969, *Aust. J. Phys.*, 22, 613.
- Murdin, P. & Clark, D. H. 1979, *MNRAS*, 189, 501.
- Murray, S. S., Slane, P. O., Seward, F. D., Ransom, S. M., & Gaensler, B. M. 2002, *ApJ*, 568, 226.
- Ostrowski, M. 1999, *A&A*, 345, 256.
- Pacholczyk, A. G. 1970, *Radio Astrophysics*, (San Francisco: Freeman).
- Pacini, F. & Salvati, M. 1973, *ApJ*, 186, 249.
- Park, S., Roming, P. W. A., Hughes, J. P., Slane, P. O., Burrows, D. N., Garmire, G. P., & Nousek, J. A. 2002, *ApJ*, 564, L39.
- Reynolds, S. P. & Chevalier, R. A. 1984, *ApJ*, 278, 630.
- Reynolds, S. P. & Gilmore, D. M. 1986, *AJ*, 92, 1138.
- Saken, J. M., Fesen, R. A., & Shull, J. M. 1992, *ApJS*, 81, 715.
- Sault, R. J. 1994, *A&AS*, 108, 55.
- Sault, R. J., Bock, D. C.-J., & Duncan, A. R. 1999, *A&AS*, 139, 387.
- Sault, R. J., & Killeen, N. E. B. 1999, *The Miriad User's Guide*, (Sydney: Australia Telescope National Facility). (<http://www.atnf.csiro.au/computing/software/miriad/>).
- Sault, R. J., Staveley-Smith, L., & Brouw, W. N. 1996, *A&AS*, 120, 375.
- Schlickeiser, R. & Fürst, E. 1989, *A&A*, 219, 192.
- Slane, P., Chen, Y., Schulz, N. S., Seward, F. D., Hughes, J. P., & Gaensler, B. M. 2000, *ApJ*, 533, L29.
- Torii, K., Tsunemi, H., & Slane, P. 1998, in *The Hot Universe. Proceedings of IAU Symposium 188*, ed. K. Koyama, S. Kitamoto, & M. Itoh, (Dordrecht: Kluwer Academic), 258.
- Truelove, J. K. & McKee, C. F. 1999, *ApJS*, 120, 299 (TM99).
- Tuohy, I. R., Clark, D. H., & Burton, W. B. 1982, *ApJ*, 260, L65.
- van den Bergh, S. 1979, *ApJ*, 234, 493.
- van der Laan, H. 1962, *MNRAS*, 124, 125.
- van der Swaluw, E., Achterberg, A., & Gallant, Y. A. 1998, *Mem. della Soc. Ast. It.*, 69, 1017.
- van der Swaluw, E., Achterberg, A., Gallant, Y. A., & Tóth, G. 2001, *A&A*, 380, 309.
- Velusamy, T., Becker, R. H., Goss, W. M., & Helfand, D. J. 1989, *J. Astrophys. Astr.*, 10, 161.
- Velusamy, T., Becker, R. H., & Seward, F. D. 1991, *AJ*, 102, 676.
- Wilson, T. L., Mezger, P. G., Gardner, F. F., & Milne, D. K. 1970, *A&A*, 6, 364.
- Woltjer, L., Salvati, M., Pacini, F., & Bandiera, R. 1997, *A&A*, 325, 295.

TABLE 1
OBSERVATIONS OF G292.0+1.8 WITH THE ATCA.

Date	Observing Freq (MHz)	Array Configuration	Time on Source (hr)	Secondary Calibrator
1994 Apr 07	1376 / 1420 ^a	375	7.5	PKS B1105-680
1994 May 04	1376 / 1420 ^a	6D	8.2	PKS B1105-680
1997 Apr 14	2240 / 2496	375	10.7	PKS B1148-671
1997 Apr 17	5056 / 5440	375	9.9	PKS B1148-671
1997 Jun 21	— / 2240	6A	12.3	PKS B1148-671
1997 Sep 05	1344 / 1420 ^a	1.5C	12.0	PKS B1148-671
1997 Sep 06	4800 / 5312	1.5C	8.5	PKS B1148-671
1997 Oct 18	1472 / 2496	750C	9.7	PKS B1148-671

^a Observations in the H I line.

TABLE 2
OBSERVED PROPERTIES OF G292.0+1.8.

Waveband (cm)	Flux Density (Jy)			Resolution (arcsec)	Sensitivity ($\mu\text{Jy beam}^{-1}$)	
	Core	Plateau	Total		Stokes <i>I</i>	Stokes <i>V</i>
20	5.5 ± 0.1	6.4 ± 0.1	11.9 ± 0.1	9.6×8.0	120	30
13	5.6 ± 0.1	5.8 ± 0.1	11.4 ± 0.1	7.2×6.2	60	60
6	5.3 ± 0.1	3.5 ± 0.1	8.8 ± 0.1	5.5×4.8	110	100

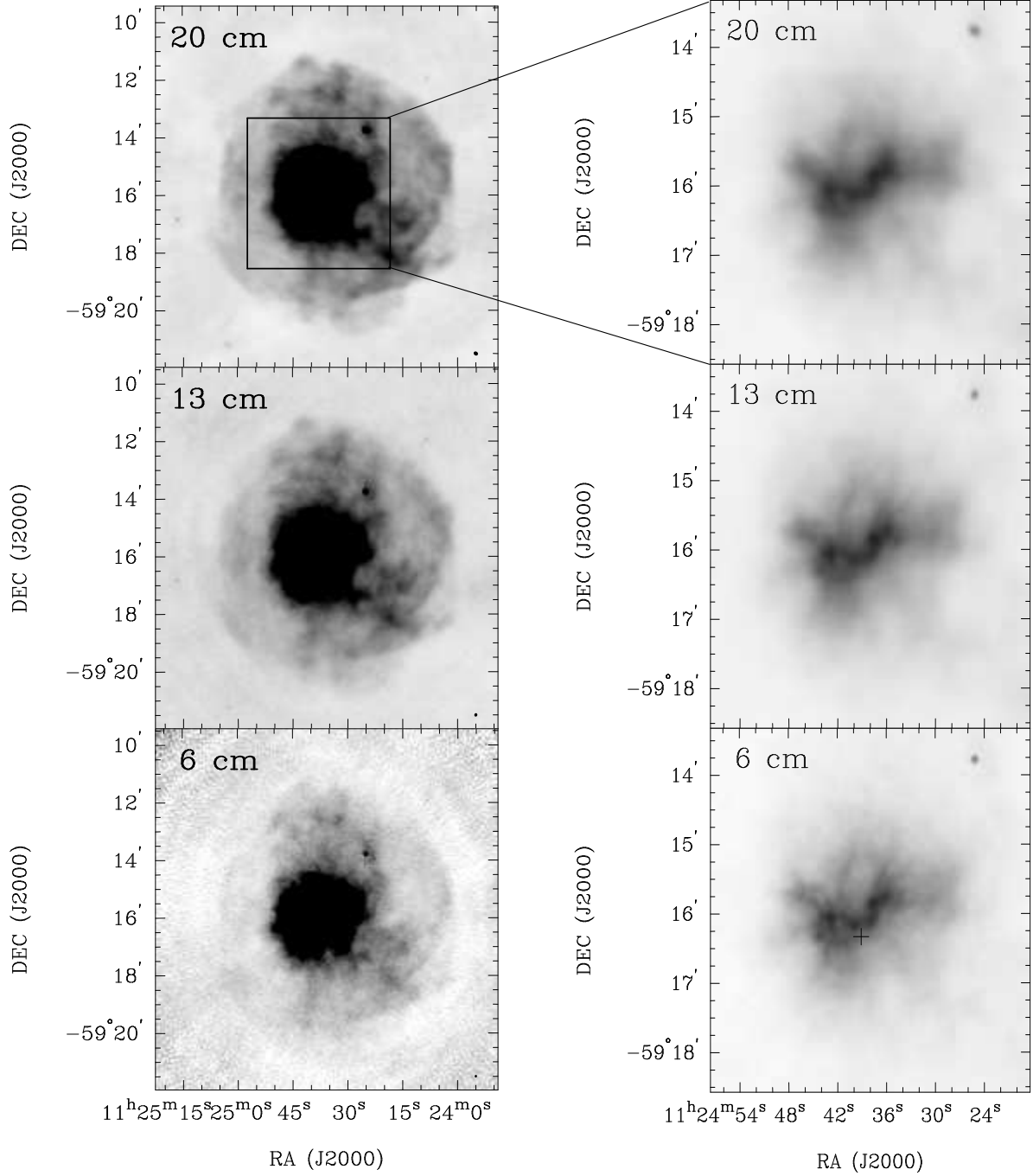


FIG. 1.— Radio continuum images of SNR G292.0+1.8 at 20, 13 and 6 cm; the left set of images shows the entire source, while the right set shows the inner core. The “+” symbol in the 6-cm image of the core marks the position of PSR J1124–5916. Each image has been corrected for primary beam attenuation; the dimensions of the synthesized beam are shown in lower right corner of the wider-field images. The greyscale ranges in the left set of images are -0.05 to $+0.5$ Jy arcmin $^{-2}$, and in the right set of images are -0.09 to $+3.5$ Jy arcmin $^{-2}$.

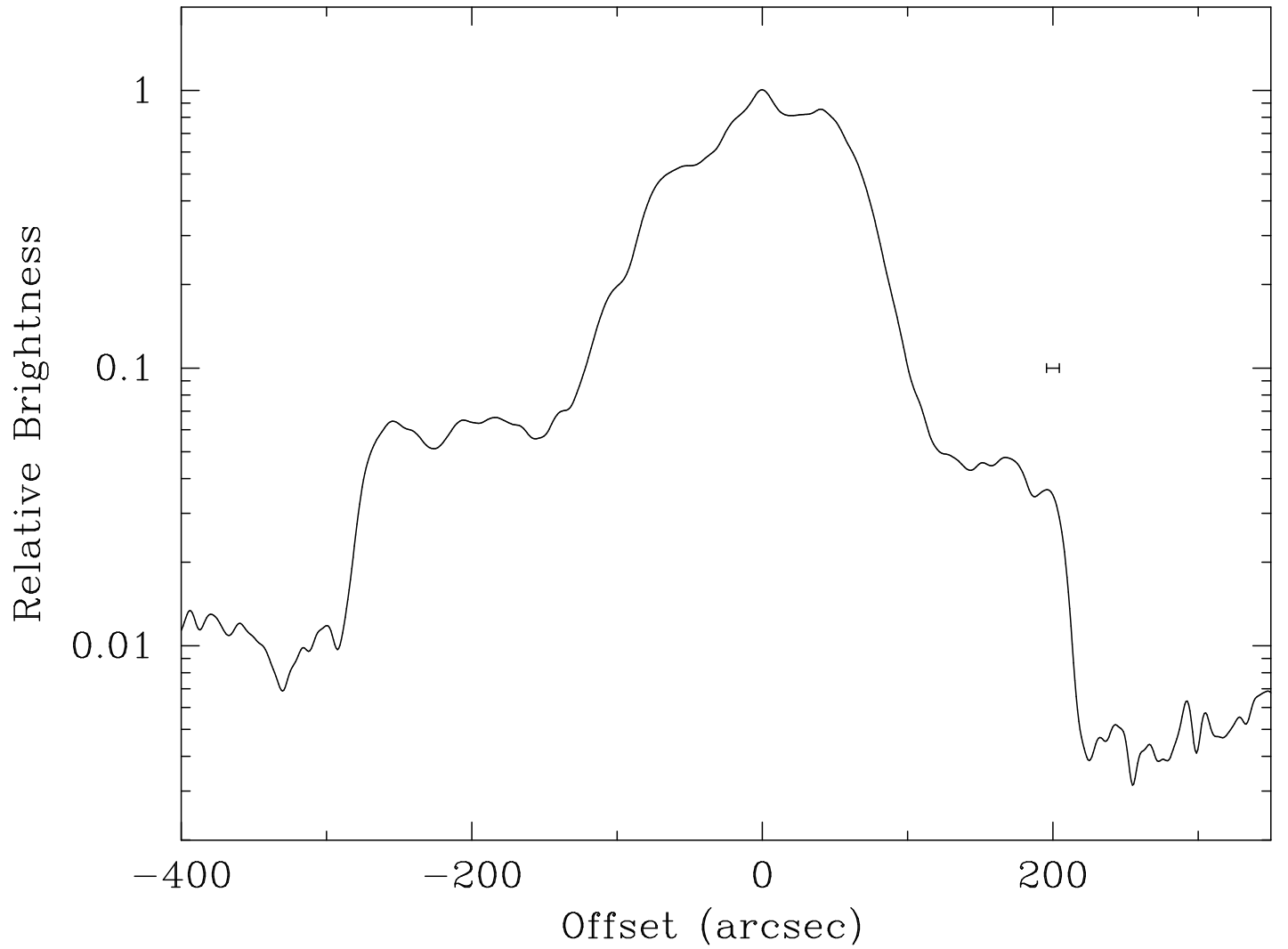


FIG. 2.— Profile of the 20-cm surface brightness of SNR G292.0+1.8. The data plotted represent an east-west slice through the SNR at a declination of (J2000) $-59^{\circ} 15' 55''.8$; the x-axis corresponds to the relative offset from the brightest pixel along this slice (positive offsets are in a westerly direction). A slight offset has been added to the surface brightness value of each datum to ensure that all values are positive before taking their logarithm. The error bar shows the FWHM of the synthesized beam.

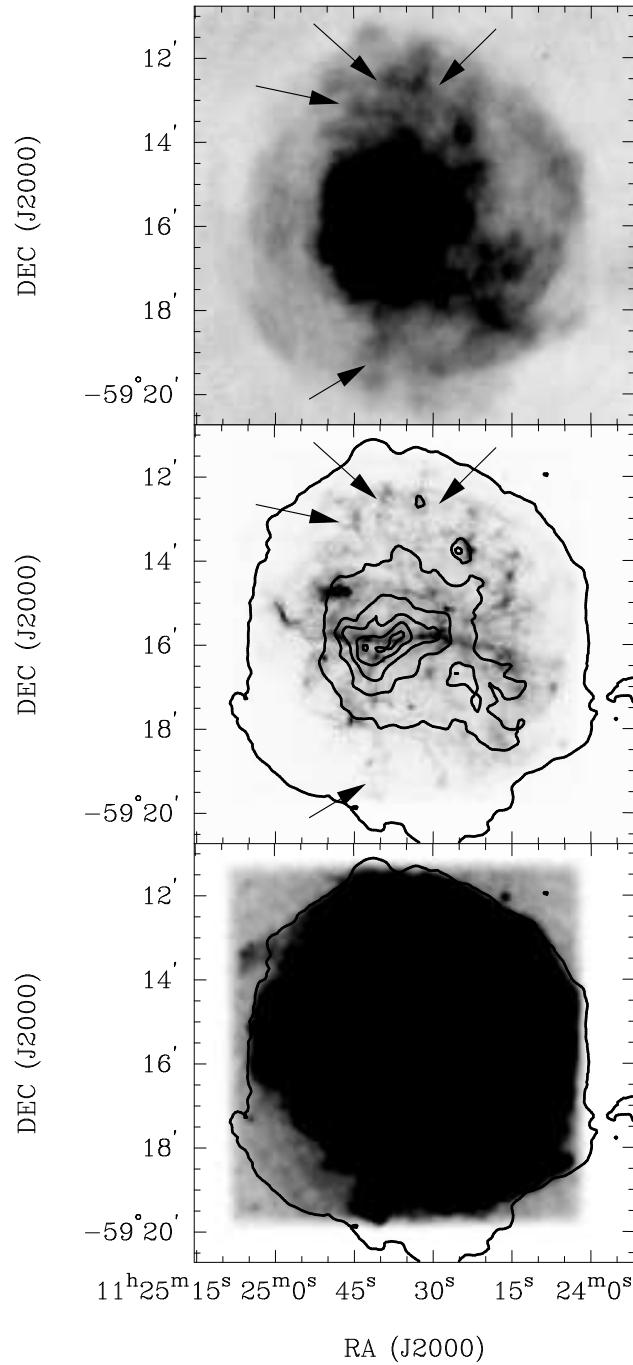


FIG. 3.— Comparison of X-ray and radio morphologies of SNR G292.0+1.8. The image in the upper panel corresponds to 13-cm ATCA data, while the lower two panels show the *Chandra* ACIS-S data of Park et al. (2002) in the energy range 0.3–10 keV. The center panel shows the morphology of the brightest X-ray emission, overlaid with 20-cm radio contours at the levels of 0.5, 5, 15, 25, 35 and 45 mJy beam⁻¹. The bottom panel has been smoothed to a resolution of 10'' and then heavily saturated to show the faintest structure; the single contour plotted represents 20-cm ATCA data at a level of 0.5 mJy beam⁻¹. The arrows in the upper two panels indicate matching radio/X-ray filaments to the north and south of the core region.

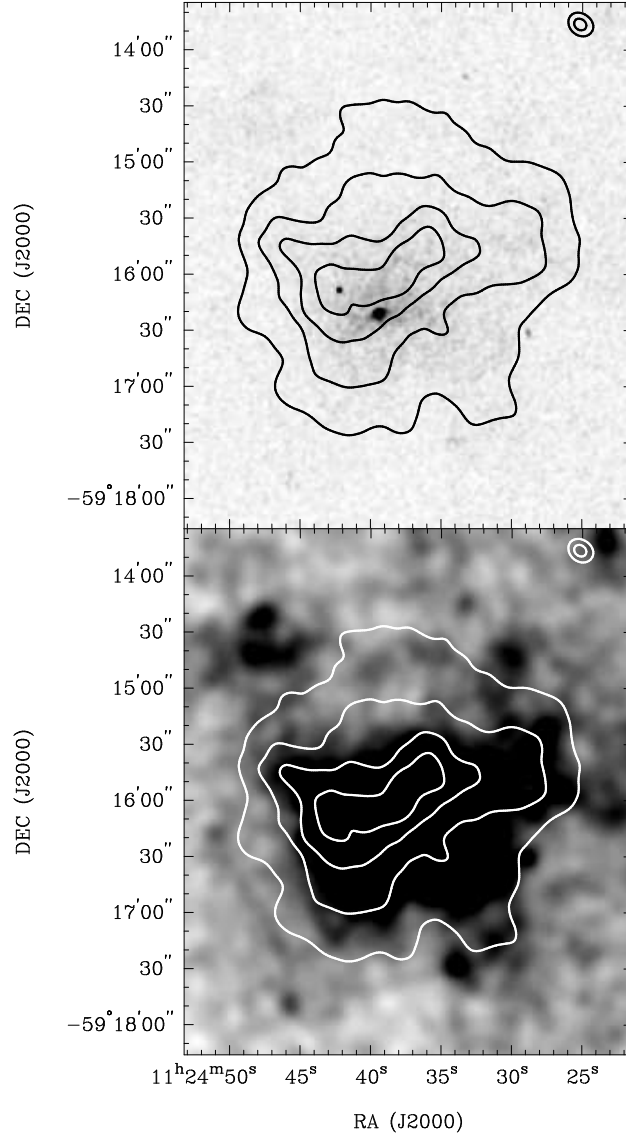


FIG. 4.— Comparison of X-ray and radio morphologies of the central region of SNR G292.0+1.8. In both panels, the greyscale shows the *Chandra* ACIS-S data of Park et al. (2002) in the energy range 2.5–10 keV, while the contours show 20-cm ATCA data at the levels of 10, 20, 30 and 40 mJy beam⁻¹. In the upper panel, the X-ray data have been smoothed with a 2'' gaussian, while in the lower panel the data have been smoothed with a 10'' and are displayed over a restricted greyscale range to bring out faint structure.

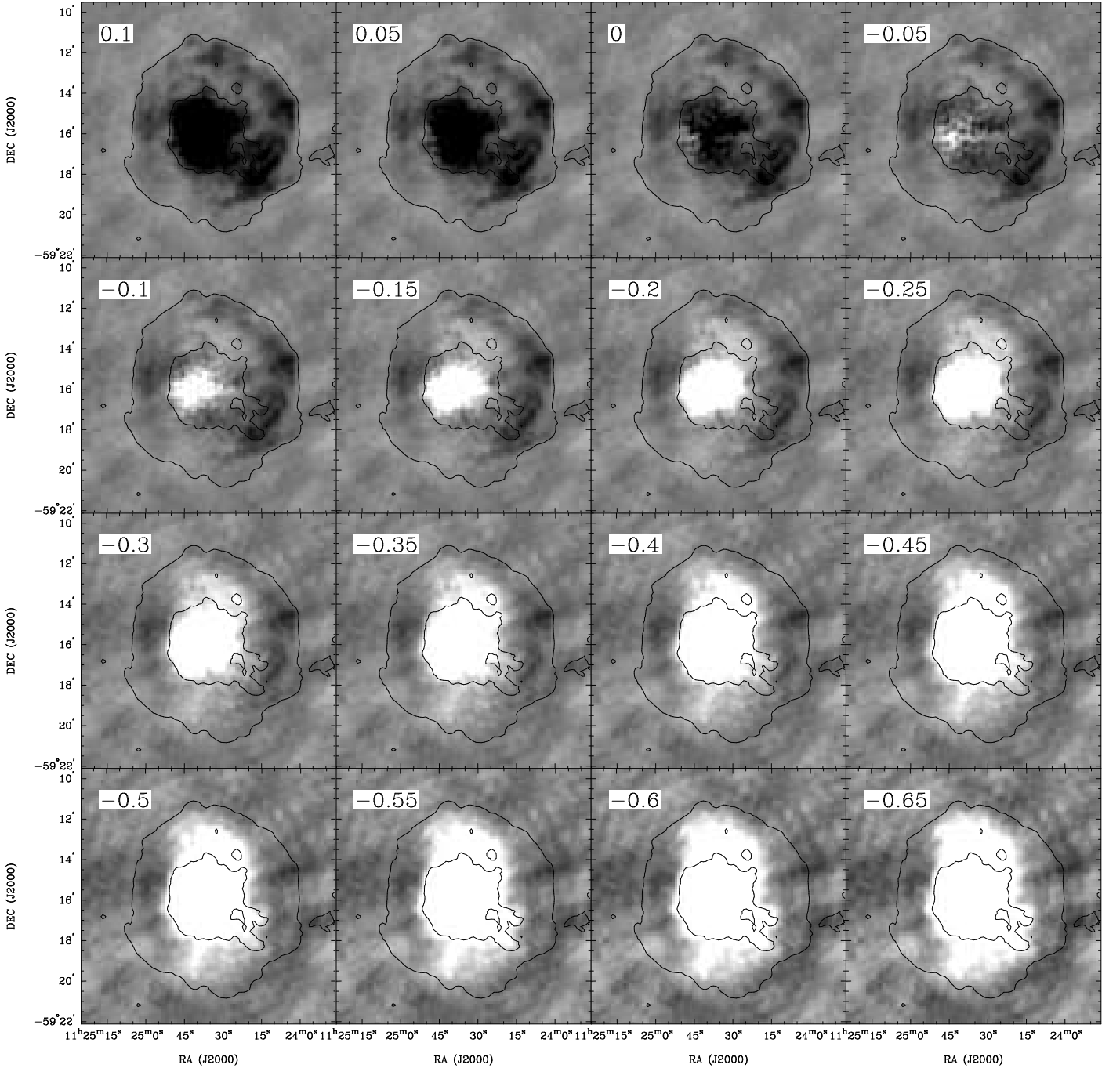


FIG. 5.— Spectral tomography images for SNR G292.0+1.8. The greyscale shows a series of difference images between 20 and 6 cm data which have been matched in $u-v$ coverage. For each panel, the trial spectral index, α_t , is shown at upper left. The data have been smoothed to a resolution of $15'' \times 15''$, and the greyscale range in each panel is -5 to $+5$ mJy beam⁻¹. The compact source at position (J2000) RA $11^{\text{h}}24^{\text{m}}25^{\text{s}}.19$, Dec $-59^{\circ}13'46''.4$ was subtracted from the 20 and 6 cm images before comparison. Overlaid are contours from the 20 cm image in Figure 1, at the levels of 0.5 and 5 mJy beam⁻¹.

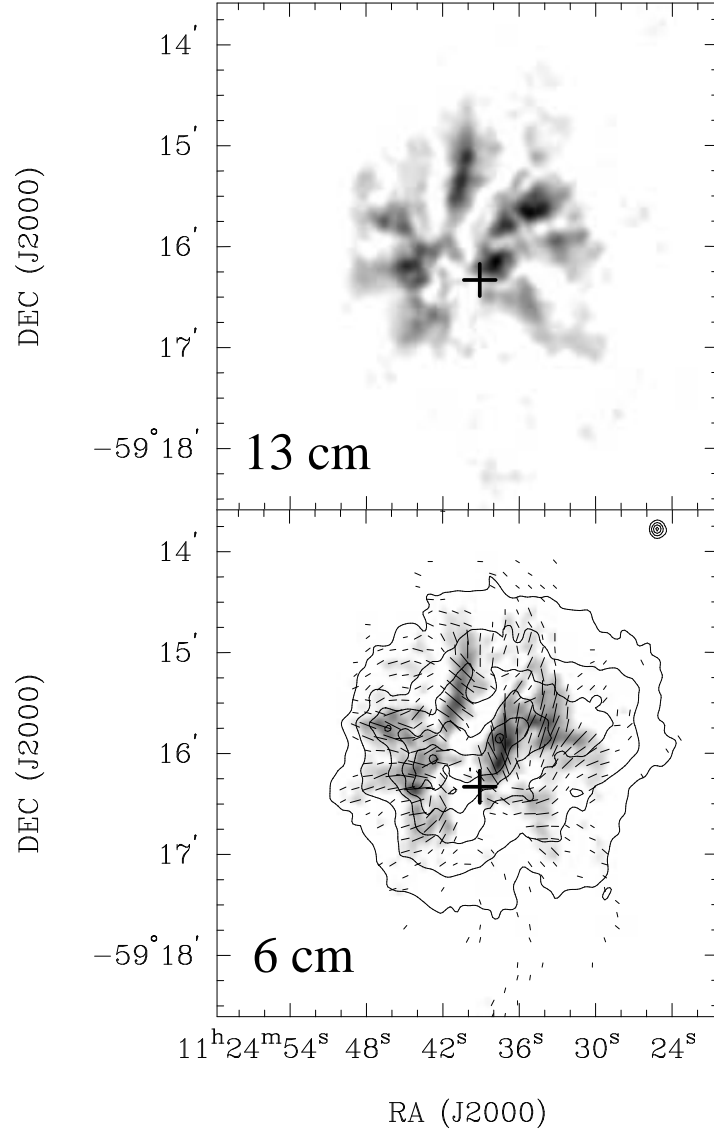


FIG. 6.— Linearly polarized emission from SNR G292.0+1.8. The upper and lower panels show polarized intensity at 13 and 6 cm respectively. In the lower panel, the image is overlaid with vectors whose length is proportional to the 6-cm polarized intensity, and whose orientation indicates the magnetic field direction after correction for Faraday rotation. The contours are 6-cm total intensity, at the levels of 2, 4, 7, 10, 13 and 16 mJy beam⁻¹. In both panels the position of PSR J1124–5916 is marked with a “+” symbol.

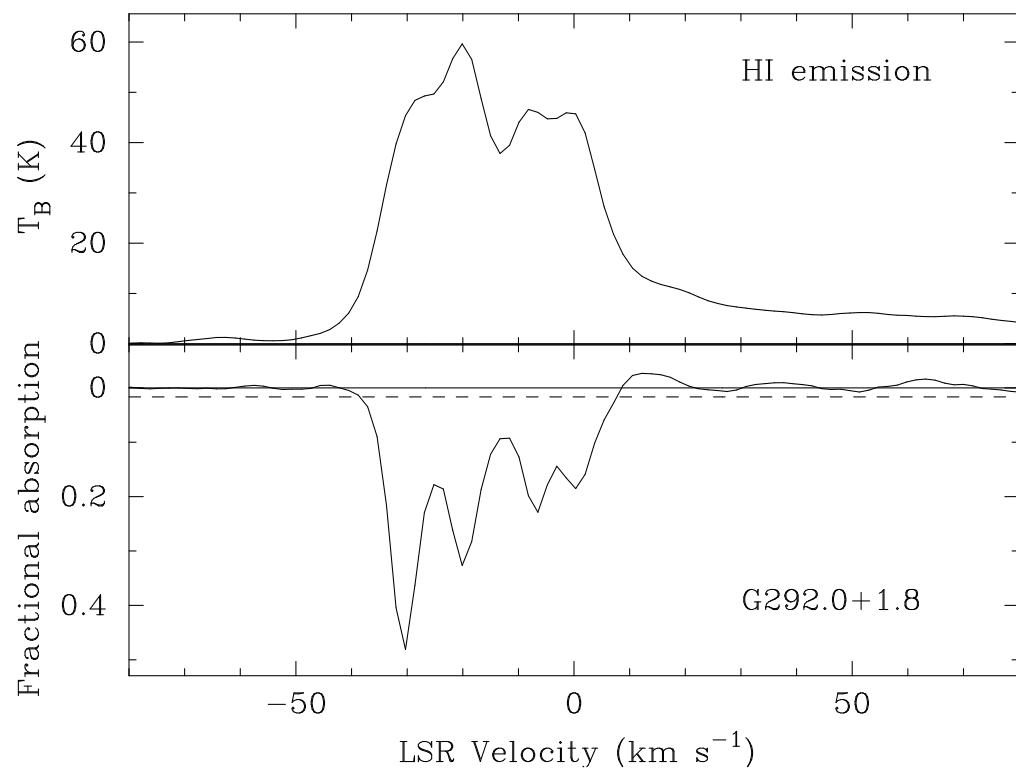


FIG. 7.— H I emission and absorption towards SNR G292.0+1.8. The upper panel shows the H I emission profile in this region, as measured by the Parkes component of the Southern Galactic Plane Survey (McClure-Griffiths et al. 2001). The lower panel shows H I absorption towards the central core of G292.0+1.8. In the lower panel, a dashed line marks absorption at the $6\text{-}\sigma$ level, where σ is calculated from the emission in line-free channels.